Original paper

From multicolored to Paraíba: the role of Mn in heat-induced color change in Cu-bearing tourmalines

Riccardo LUPPI[1*], Henrik SKOGBY[2], Federico PEZZOTTA[3], Ulf HÅLENIUS[2],

Francesco DI BENEDETTO[4], Alfonso ZOLEO[5], Ferdinando BOSI[1]

[1] *Department of Earth Sciences, Sapienza University of Rome, P. Aldo Moro, 5, I-00185 Rome, Italy; riccardo.luppi@uniroma1.it*
[2] *Department of Geosciences, Swedish Museum of Natural History, Box 50007, SE-10405 Stockholm, Sweden*
[3] *MUM – Mineralogical Museum "Luigi Celleri", Via Cavour 73, San Piero in Campo, Campo nell'Elba, Livorno, Italy*
[4] *Department of Physics and Earth Science, University of Ferrara, Via Saragat 1, Ferrara, Italy*
[5] *DiSC, Dipartimento di Scienze Chimiche, Università degli Studi di Padova, Via Marzolo, 1, 35131 Padova, Italy*
[*] *Corresponding author*

Tourmalines, with their wide range of colors, are among the most sought-after and highly valued minerals in the gemstone market. For this reason, they are often subjected to laboratory treatments to enhance their color. Among the rarest and most expensive tourmaline varieties, the Cu-bearing Paraíba tourmaline stands out for its distinctive and unique neon blue color. In this study, we investigate a multicolored Cu-bearing tourmaline from the Mavuco deposit in Mozambique. The studied sample is compositionally identified as fluor-elbaite. Electron microprobe analysis, optical absorption, Fourier-transform infrared, and electron paramagnetic resonance spectroscopy are used to clarify the causes of its natural color zoning and the mechanisms underlying color changes induced by heat treatment. The untreated crystal exhibits distinct color zones: a dark green root (R1), a yellowish light green band (R2), intermediate light blue (I1) and blue violetish (I2) zones, and a greyish violet terminal portion (T). Chemical analyses show that Fe, Mn, Cu, and Ti concentrations change systematically along the crystal, with Fe^{2+}/Fe^{3+} exchange-coupled pairs interactions and Fe^{2+}–Ti^{4+} intervalence charge transfer (IVCT) controlling the dark green color of the crystal root (R1), while Mn^{2+}–Ti^{4+} IVCT and Fe^{2+}–Ti^{4+} IVCT producing the yellowish light green color (R2). Cu^{2+} is the only chromophore in the light blue (I1) zone, classifying it as a natural Paraíba-type tourmaline. In the blue violetish (I2) and greyish violet (T) zones, the presence of Mn^{3+} is likely the result of an interaction with localized natural radioactive fluids, and in combination with Cu^{2+} absorptions produces violetish color. The heat treatment under reducing conditions (~500 °C, 18 h) selectively reduces Mn^{3+} to Mn^{2+}, homogenizing the color of the intermediate (I2) and terminal (T) zones to light blue. The resulting Paraíba-like color is therefore attributed solely to Cu^{2+}.

This study demonstrates that the color of Cu-bearing tourmalines is governed by the combination, concentration and oxidation state of Cu, Mn, Fe and Ti, as well as by post-crystallization redox processes. It also highlights the importance of tourmaline color as a petrogenetic recorder of subtle physicochemical changes in its crystallization environment. These findings provide interesting insights into pegmatitic evolution, the role of natural irradiation in gemstone coloration, and the gemological distinction between natural and treated Paraíba-type tourmalines.

Keywords: tourmaline, thermally treated, chemical analyses, spectroscopic analyses
Received: December 29, 2025; accepted: June 17, 2026; handling editor: P. Bačík
The online version of this article (doi: 10.3190/jgeosci.0058.25) contains supplementary electronic material.

1. Introduction

Tourmalines are a supergroup of chemically complex borosilicates (e.g., Ertl et al. 2002; Agrosì et al. 2006; Henry and Dutrow 2011; Bosi 2018), whose general formula may be written as $XY_3Z_6T_6O_{18}(BO_3)_3V_3W$ (Henry et al. 2011), where X = Na, K, Ca, □ (= vacancy); Y = Al, Fe^{3+}, Cr, V, Mn^{3+}, Mg, Fe^{2+}, Mn^{2+}, Li, Ti, Cu; Z = Al, Fe^{3+}, Cr, V, Mg, Fe^{2+}; T = Si, Al, B^{3+}; B = B^{3+}; V = (OH), O; W = (OH), F, O. Note that the not italicized letters X, Y, Z and B represent groups of cations at the $^{[9]}X$, $^{[6]}Y$, $^{[6]}Z$, $^{[4]}T$ and $^{[3]}B$ crystallographic sites (letters italicized). The letters V and W represent groups of anions accommodated at the [3]-coordinated O(3) and O(1) crystallographic sites, respectively. Tourmalines are classified into three groups based on the occupancy of the *X* site: the vacancy group, the alkali group, and the calcic group (Henry et al. 2011).

The evolution of the physicochemical conditions of the pegmatitic fluid during crystallization is recorded in internal compositional variations, which in tourmaline typically manifest as color zoning (e.g., Dutrow and Henry 2018). Moreover, tourmalines represent an excel-

Published under Creative Commons Attribution-NonCommercial 4.0 International (CC BY-NC 4.0) license

lent example of mineral color variability, exhibiting tones across the entire visible spectrum. These colors arise through various mechanisms, including crystal field transitions, intervalence charge transfer interactions (IVCT), and color centers (Fritsch and Rossman 1987; Pezzotta and Laurs 2011; Rossman 2014). Specifically, transition metals such as Ti, V, Cr, Mn, Fe, Ni and Cu, located at the *Y* and *Z* sites, act as primary chromophores, influencing both tone and saturation of the color (Rossman et al. 1991; Pezzotta and Laurs 2011; Li et al. 2018). However, defects induced by impurities and polyhedral distortions were also invoked to affect color (Li et al. 2018).

The most appreciated variety of tourmaline for its bright colors, ranging from turquoise green to neon blue, is Paraíba. This rare Cu-bearing tourmaline, found in Brazil, Nigeria, Mozambique, and Ethiopia is currently one of the most expensive gemstones on the market (Pezzotta and Laurs 2011). For this reason, Cu-bearing tourmalines of less desirable colors, particularly purple, are commonly subjected to heat treatment to produce the characteristic Paraíba neon blue. Understanding the natural causes of color, as well as the mechanisms responsible for color variations induced by heat treatment, is therefore important for accurately distinguishing between natural coloration and treatment-induced ones.

In this study, a multicolored Cu-bearing tourmaline from the Mavuco deposit, located in the Alto Ligonha pegmatite district (NE Mozambique), was subjected to controlled heat treatment and comprehensive chemical and spectroscopic characterization using electron microprobe analysis (EMPA), Fourier-transform infrared spectroscopy (FTIR), optical absorption spectroscopy (OAS), and electron paramagnetic resonance (EPR) spectroscopy. By investigating this multicolored sample, representative of the entire range of colors exhibited in the deposit, we aimed to explain both the color mechanisms in the untreated sample and the chromatic changes induced by heating. It was also attempted to clarify potential changes in the tourmaline crystallization environment by investigating the causes of the localized redox change affecting Mn in the purple zone of the untreated crystal.

2. Geological setting

The secondary deposit of Mavuco is a mining area of over 12 km^2 located in the Nampula Province, in the Alto Ligonha pegmatite district, northeastern Mozambique (Laurs et al. 2008). The area, adjacent to the village of Mavuco, lies approximately 95 km south–southwest of the city of Nampula. Geographically, the region marks a transition between low coastal plains in the southeast and elevated plateaus toward the northwest, with the local landscape characterized by mostly flat terrain interrupted by the prominent granite inselbergs of Mt. Muli, rising to ~600 m (Laurs et al. 2008). Geologically, the basement rocks in the Mavuco area are part of the Mozambique Belt, a Neoproterozoic orogenic belt dated to 1,100–800 Ma, which extends from the Mediterranean Sea to central Mozambique (Lächelt 2004; Laurs et al. 2008). The basement consists of strongly metamorphosed gneisses and migmatites, largely deformed during the Pan-African event (~800–550 Ma). Between 600 and 410 Ma, this basement was intruded by granitoids and numerous rare-element granitic pegmatites, particularly abundant within ~200 km of the Alto Ligonha region. These pegmatites, mined since the 1930s, host significant concentrations of rare metals and gem minerals including tourmaline and beryl (Bettencourt Dias and Wilson 2000; Lächelt 2004; Laurs et al. 2008). The entire Mavuco area is affected by the tropical weathering, with most of the surface mantled by a thick lateritic soil. The local bedrock consists of various types of gneiss, as well as the granites of Mt. Muli and Mt. Iulùti. Laurs et al. (2008) reported that simple granitic pegmatites locally crosscutting these basement rocks are Li-poor, and therefore they cannot be considered the source of Cu-bearing tourmaline. The same authors reported that Cu-bearing tourmaline is found exclusively in secondary deposits, forming a layer of waterworn pebbles that rests directly on weathered biotite gneiss, known locally as *kamada*, interpreting the deposit as a paleoplacer.

As reported in Altieri et al. (2024), *kamada* consists of a several centimeters to 1 m thick unit where tourmalines occur as sub-angular to sub-rounded fragments, typically ranging from 1 g to over 100 g, set within a residual soil level mostly composed of quartz fragments, with subordinate feldspar, beryl, and spessartine. This *kamada* layer occurs on top of the altered bedrock, which generally consists of amphibolitic paragneiss, and more rarely of marble lenses, as well as aplitic and pegmatitic veins. Above the *kamada* lies the *kororo*, a reddish to brownish lateritic soil ranging from 1 m to over 10 m in thickness, composed largely of bauxitic material with iron hydroxide nodules, sparse small quartz grains, and lacking gem minerals (Altieri et al. 2024).

During recent years, systematic observations on the soil sections exposed during the mechanized excavations, argue for an eluvial to locally colluvial origin as the distribution and the thickness of the *kamada* are not related to the morphology and hydrology of the land (Pezzotta 2018; Altieri et al. 2024). The persistence of the *kamada* layer, its lack of correlation with surface drainage patterns, the presence of clasts with well-preserved crystal faces, and the local thickening of the *kamada* above altered quartz and pegmatitic veins in the bedrock all support in situ weathering of a primary pegmatitic system, likely still present at depth. Ongoing work aims to refine this residual-origin model.

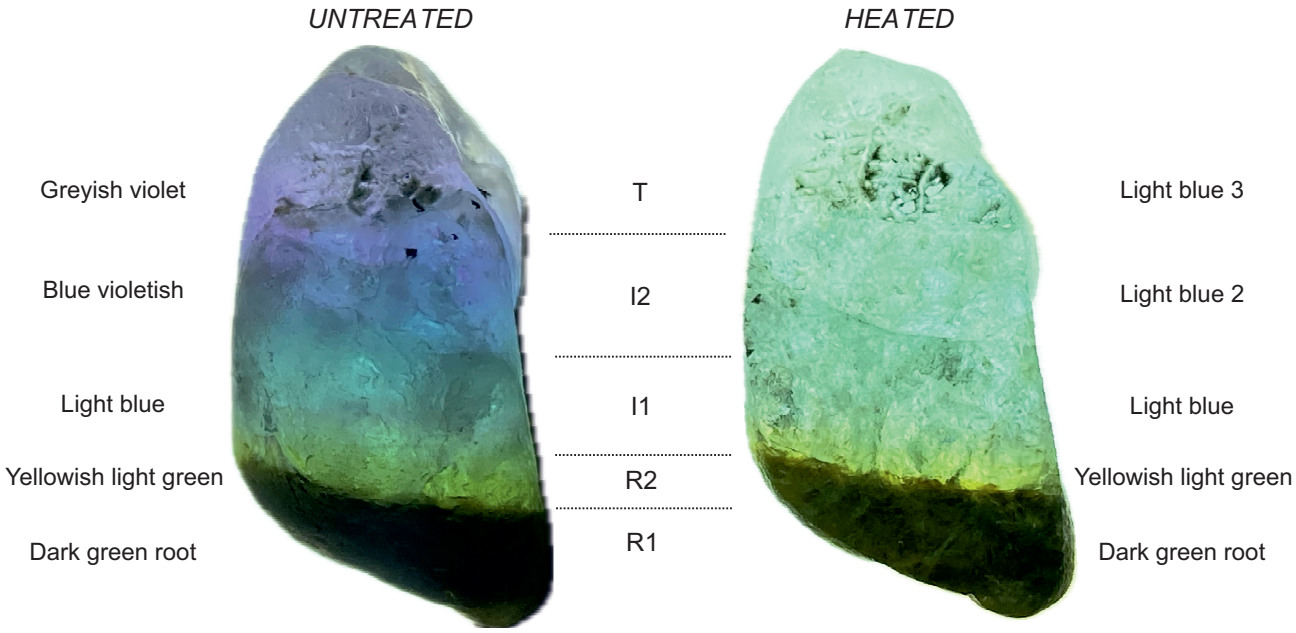


Fig. 1 Multicolored Cu-bearing tourmaline from the Mavuco deposit (Mozambique), shown before and after heat treatment, with classification of the various color zones.

3. Materials and Analytical Methods

3.1. Samples

The studied specimen, labelled as 3_3, is a multicolored, residual, sub-rounded Cu-bearing tourmaline collected from the Mavuco area in the Alto Ligonha pegmatite district, northeastern Mozambique (Fig. 1). The sample, measuring approximately 1.6 × 0.5 cm, was cut into two halves: one half was used as the untreated reference, while the other was subjected to heat treatment under reducing conditions at approximately 500 °C for 18 hours (Fig. 1). The lengths of the untreated and heat-treated sections, measured parallel to the **c**-axis, are approximately 17,000 µm and 15,000 µm, respectively. Color classification was performed using the Munsell system, under both transmitted and incident light, observed parallel and perpendicular to the **c**-axis, before and after the heating cycle. The untreated sample exhibits different color gradations, which can be simplified into five main color zones extending from the crystal root to the termination: dark green (R1), yellowish light green (R2), light blue (I1), blue violetish (I2), and finally greyish violet (T) (Fig. 1). This color gradation is similar to that reported in Fig. 2 of Altieri et al. (2024) but lacks the final dark green overgrowth. Moreover, in the studied sample the **c**-axis is oriented roughly parallel to the elongation of the fragment; for this reason, we refer to the section as extending from root to termination rather than from core to rim.

After heat treatment, the color of the sample became largely homogenized into a greenish light blue shade, except for the crystal root, which remained dark green with an overlying yellowish light green band. Chemical and spectroscopic data (EMPA, FTIR, OAS and EPR) were acquired on both untreated and heat-treated sections to better understand the redox process involved in the color mechanisms.

3.2. Chemical analysis

Electron microprobe analyses were carried out using a JEOL JXA-iSP100 Super Probe instrument at the joint CNR (IGAG)–Sapienza laboratory at the Department of Earth Sciences at the Sapienza University of Rome. Compositional data were collected along a straight traverse parallel to the **c**-axis, using wavelength dispersive spectrometers (WDS mode) with an accelerating potential of 15 kV, a sample current of 10 nA, 1 µm beam diameter and a working distance of 11 mm. The PAP routine was applied (Pouchou and Pichoir 1991). Minerals and synthetic compounds were used as standards: chromite (Fe$K\alpha$), Mn (Mn$K\alpha$), Cu (Cu$K\alpha$), albite (Na$K\alpha$), diopside (Mg$K\alpha$), fluorapatite (F$K\alpha$), wollastonite (Ca$K\alpha$, Si$K\alpha$), ilmenite (Ti$K\alpha$), factory-calibrated standard (Ni$K\alpha$), orthoclase (K$K\alpha$, Al$K\alpha$), Zn (Zn$K\alpha$), chromite (Cr$K\alpha$), Co (Co$K\alpha$), Pb glass (Pb$M\alpha$) and factory-calibrated standard (V$K\alpha$). Magnesium, V, Cr, K, Zn, Ni, Ba, Cl, Co, Cs, Sb, N, and Rb were below detection limits (< 0.03 wt. %). Tables 1 and 2 report the average of 40 and 38 spots measured on the untreated and heat-treated samples, respectively.

Tab. 1 Average compositions from EMPA and atoms per formula unit (*apfu*) for the different coloured zones of the 3_3 untreated Cu-bearing multicolored tourmaline

Constituent (wt. %)	R1 n = 9	R2 n = 4	I1 n = 9	I2 n = 9	T n = 9
SiO_2	38.89(75)	39.11(16)	39.10(45)	39.28(63)	38.29(36)
TiO_2	0.12(4)	0.05(1)	0.01(2)	0.01(1)	0.01(1)
$B_2O_{3(calc)}$	11.18	11.25	11.32	11.36	11.11
Al_2O_3	40.80(74)	41.53(60)	42.49(24)	42.64(68)	41.62(35)
FeO	1.81(14)	0.40(12)	0.03(6)	–	0.01(1)
MnO	0.49(6)	0.54(24)	0.06(6)	–	0.11(2)
Mn_2O_3*	–	–	–	0.08(4)	0.13(2)
CuO	0.05(3)	0.14(3)	0.26(5)	0.30(10)	0.16(5)
MgO	0.01(1)	–	–	–	–
CaO	0.20(8)	0.41(15)	0.18(1)	0.40(9)	0.21(13)
Na_2O	2.15(13)	2.00(6)	1.96(10)	1.89(12)	1.94(7)
K_2O	0.02(1)	0.02(1)	0.02(1)	0.02(1)	0.02(1)
Li_2O**	1.84	2.02	2.05	2.05	2.03
F	1.05(17)	1.57(50)	1.26(12)	1.25(26)	1.01(10)
H_2O_{calc}	3.19	3.00	3.23	3.15	3.29
O = F	–0.44	–0.66	–0.53	–0.53	–0.43
Total	101.41	101.40	101.48	101.93	99.52

APFU	R1	R2	I1	I2	T
Si	6.046	6.040	6.002	6.010	5.993
Ti^{4+}	0.013	0.006	0.001	0.001	0.001
B	3.000	3.000	3.000	3.000	3.000
Al	7.477	7.561	7.688	7.690	7.676
Fe^{2+}	0.235	0.051	0.004	0.001	–
Mn^{2+}	0.065	0.070	0.008	–	0.015
Mn^{3+}	–	–	–	0.010	0.017
Cu	0.006	0.016	0.030	0.035	0.019
Mg	0.002	–	–	–	–
Ca	0.033	0.068	0.029	0.066	0.035
Na	0.649	0.599	0.583	0.562	0.587
K	0.004	0.004	0.004	0.003	0.004
Li	1.151	1.255	1.266	1.262	1.278
F	0.516	0.767	0.612	0.605	0.500
OH	3.308	3.090	3.304	3.217	3.439

* From Optical Absorption spectroscopy
** From Pesquera et al. 2016

3.3. Infrared spectroscopy

Fourier-transform infrared (FTIR) spectroscopy was used to characterize the (OH) vibrational absorption bands of the sample before and after the heat treatment. The spectrometer system consisted of a Bruker Vertex 70 spectrometer equipped with a halogen-lamp source and a CaF_2 beam-splitter coupled to a Hyperion 2000 microscope with a ZnSe wire-grid polarizer and an InSb detector at the Department of Geosciences, Swedish Museum of Natural History. Polarized spectra were collected parallel and perpendicular to the **c**-axis over the wavenumber range 2,000–13,000 cm^{-1} with a resolution of 4 cm^{-1}.

3.4. Optical absorption spectroscopy (OAS)

Polarized room temperature optical absorption spectra parallel and perpendicular to the **c**-axis were acquired at the Department of Geosciences, Swedish Museum of Natural History in Stockholm, using an AVASPEC-ULS2048 × 16 spectrometer connected via a 400 µm ultraviolet (UV) optical fiber cable to a Zeiss Axiotron UV microscope. A 75 W Xenon arc lamp was used as a light source and Zeiss Ultrafluar 10× lenses served as objective and condenser. UV-grade Glan-Thompson prism, with a working range of 40,000 to 3,704 cm^{-1} was used as the polarizer. OAS analyses were obtained in the range 30,000–11,500 cm^{-1} with a spectral resolution of

Tab. 2 Average compositions from EMPA and atoms per formula unit (*apfu*) for the different coloured zones of the 3_3 heated Cu-bearing tourmaline

Constituent (wt. %)	R1 n = 7	R2 n = 4	I1 n = 9	I2 n = 10	T n = 8
SiO_2	38.87(25)	38.93(45)	39.25(27)	39.29(84)	38.88(93)
TiO_2	0.13(3)	0.02(2)	–	0.01(1)	–
$B_2O_{3(calc)}$	11.16	11.22	11.36	11.37	11.26
Al_2O_3	40.59(28)	41.56(58)	42.69(26)	42.68(70)	42.17(94)
FeO	1.81(13)	0.40(11)	0.04(6)	0.01(1)	0.01(1)
MnO	0.57(6)	0.50(26)	0.04(4)	0.06(4)	0.16(2)
Mn_2O_3*	–	–	–	–	–
CuO	0.07(2)	0.09(3)	0.22(7)	0.28(7)	0.24(4)
MgO	0.01(1)	–	–	–	–
CaO	0.27(2)	0.31(12)	0.12(6)	0.29(8)	0.33(3)
Na_2O	2.17(10)	1.97(11)	1.94(7)	1.85(19)	1.78(23)
K_2O	0.02	0.02(1)	0.02(1)	0.02(1)	0.02
Li_2O**	1.85	2.00	2.04	2.05	2.05
F	1.20(30)	1.25(19)	1.22(27)	1.06(30)	1.22(27)
H_2O_{calc}	3.10	3.17	3.26	3.33	3.25
O = F	–0.51	–0.53	–0.51	–0.45	–0.51
Total	101.38	100.96	101.73	101.89	100.88

APFU	R1	R2	I1	I2	T
Si	6.053	6.031	6.007	6.006	6.003
Ti^{4+}	0.015	0.002	–	0.001	–
B	3.000	3.000	3.000	3.000	3.000
Al	7.450	7.588	7.700	7.690	7.673
Fe^{2+}	0.235	0.052	0.005	0.001	0.001
Mn^{2+}	0.075	0.066	0.005	0.008	0.020
Mn^{3+}	–	–	–	–	–
Cu	0.008	0.011	0.025	0.032	0.028
Mg	0.002	–	–	–	–
Ca	0.045	0.051	0.019	0.048	0.054
Na	0.654	0.591	0.576	0.548	0.533
K	0.004	0.003	0.003	0.005	0.004
Li	1.159	1.246	1.256	1.260	1.273
F	0.591	0.612	0.590	0.512	0.596
OH	3.222	3.277	3.325	3.395	3.348

* From Optical Absorption spectroscopy
** From Pesquera et al. 2016

1 nm. Spectral data in the range 11,500–5,000 cm^{-1} were taken from FTIR measurements (Figs 3 and 4).

3.5. Electron Paramagnetic Resonance spectroscopy (EPR)

The EPR spectral measurements were carried out using a conventional Bruker ECS106 X-Band CW EPR spectrometer, available at the Department of Chemical Sciences of the University of Padua (Italy), operating at ~9.5 GHz (X-band). Spectra were registered at room temperature, under the following operating conditions: 0.2 mT modulation amplitude, 100 kHz modulation frequency. Two samples were considered: a fragment from the terminal T portion of the untreated tourmaline 3_3 (EPR_r), and a fragment from the terminal T portion of the heat-treated one (EPR_t). For EPR_t, spectra were acquired in a wide field range (48–648 mT) with 8192 pts (corresponding to 0.073 mT/pt) for different orientations of the sample with respect to the magnetic field. Indeed, since the sample was a single crystal, different orientations of the sample with respect to the applied magnetic field, corresponded to possible different magnetic parameters A and g of the paramagnetic centers.

For the EPR_r sample, a spectrum was acquired in a single orientation with the same previous conditions. Then, spectra were acquired for different orientations in a narrow field range (260–360 mT), where just the signals of interest were expected. No smoothing or noise reduction was applied to the

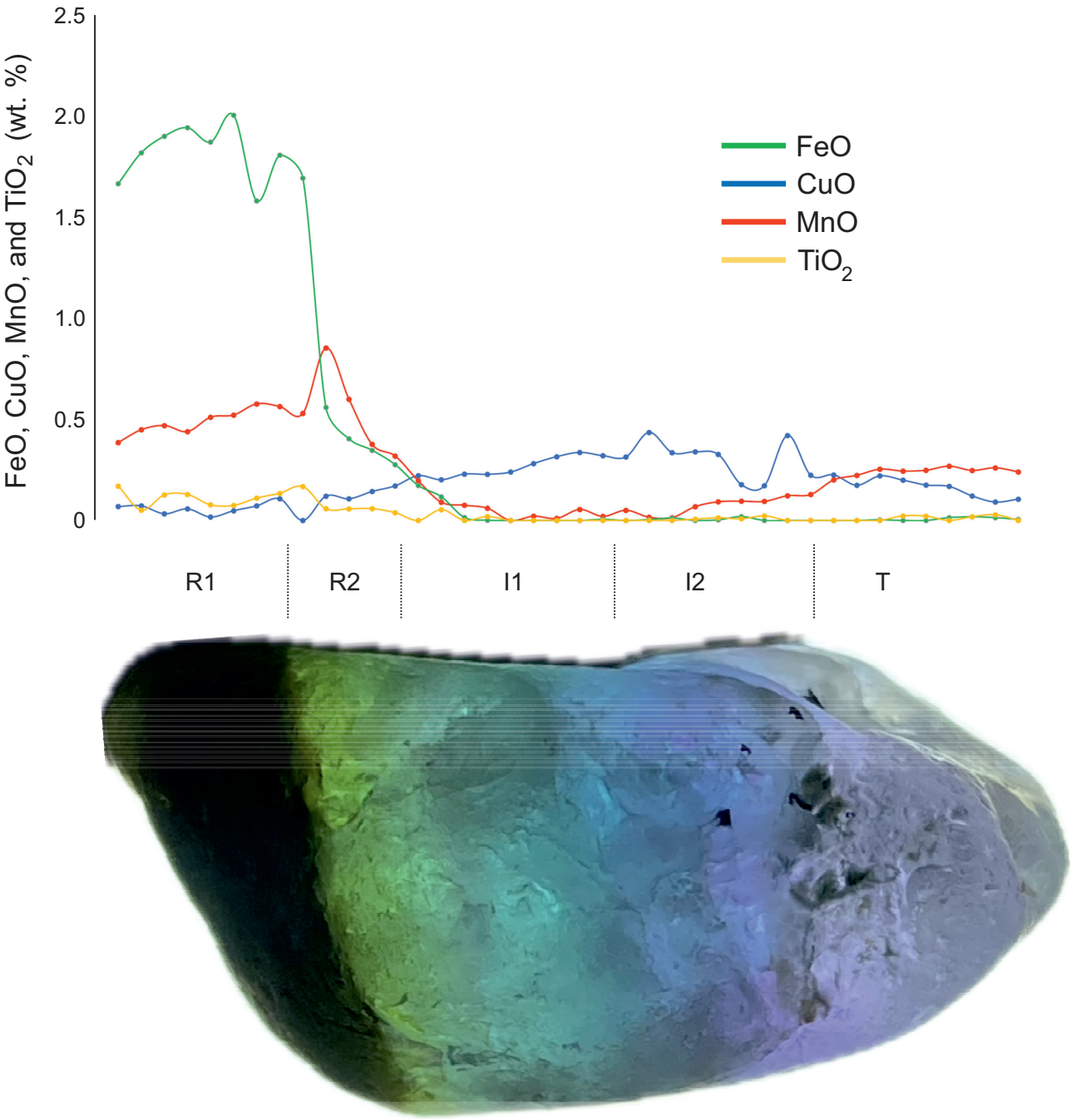


Fig. 2 Trend of selected oxides from the root (R1) to the terminal portion (T) in the untreated multicolored Cu-bearing tourmaline sample, based on data obtained from EMPA analysis.

spectra to preserve the integrity of the diagnostic spectral parameters. To better assess and discriminate the Mn^{2+} and Cu^{2+} signals, a small fragment of the EPR_t was powdered and examined both in Q-band and X-band, and the spectra were simulated to get the A and g values of the paramagnetic centers.

4. Results

4.1. Chemical Composition

The concentrations of selected elements (expressed as wt. % oxides) measured along the traverse are shown in Fig. 2. The average compositions for each color zone

of the untreated multicolored sample, based on a total of 40 analytical points, are summarized in Tab. 1. In general, the untreated multicolored sample revealed significant variations in Fe, Mn, Cu and Ti concentrations, reflected in color changes from the dark green root (R1), through yellowish light green (R2), light blue (I1), blue violetish (I2), to slightly greyish violet (T) toward the crystal termination (Fig. 2; Tab. 1). Calcium and F also show some variability (Tab. 1). CaO reaches maximum values in the R2 (0.41 wt. %) and I2 (0.40 wt. %) zones, decreasing in I1 (0.18 wt. %), R1 (0.20 wt. %), and T (0.21 wt. %) zones. F follows a similar trend, peaking in R2 (1.57 wt. %), remaining fairly constant in the I1–I2 (1.25 wt. %) zones, and declining in the T (1.01 wt. %) and R1 (1.05 wt. %) zones (Tab. 1).

In detail, the dark green crystal root (R1), together with the overlying yellowish light green (R2) band, displays the highest Fe and Mn concentrations, with FeO ranging from 1.81 to 0.40 wt. % and MnO from 0.49 to 0.54 wt. %, respectively (Fig. 2). Titanium contents change from 0.12 wt. % TiO_2 in the R1 root to 0.05 wt. % in the R2 zone. Copper, in contrast, shows values between 0.05 and 0.14 wt. % CuO, respectively (Fig. 2; Tab. 1). In the light blue (I1) and blue violetish (I2) intermediate zones, a progressive decrease in Fe and Ti is observed, with FeO and TiO_2 contents approaching or falling below 0.03 wt. %. MnO also decreases to values close the detection limit, reaching maxima of ca. 0.08 wt. %. The copper contents, however, slightly increase to 0.26 and 0.30 wt. % CuO, respectively. In the slightly greyish violet (T) terminal portion, FeO and TiO_2 concentrations are nearly zero. Copper decreases relative to the I1 and I2 zones, with CuO values up to 0.16 wt. %, whereas MnO increases to ~0.24 wt. %.

A very similar trend was observed in the heat-treated sample, where the root portion (R1) remained dark green, overlain by a yellowish light green (R2) band, while the rest of the crystal (I1, I2 and T) turned light blue after heating (Fig. 1). Table 2 reports the average compositions, which are very similar to those of untreated sample (Tab. 1).

4.2. OAS spectra

The optical absorption spectra of the untreated and heat-treated samples were recorded in the UV-Vis-NIR region both parallel (**E||c**), and perpendicular (**E⊥c**) to the **c**-axis (Figs 3 and 4). In the 3_3 untreated multicolored sample, the spectrum of the dark green root (R1) recorded perpendicular to the **c**-axis shows strong absorption bands at approximately 13,800 cm^{-1} and 9,200 cm^{-1}, as well as a broad band near 24,000 cm^{-1} (Fig. 3). Above the R1 root, in the yellowish light green (R2) portion OAS spectrum exhibits very weak absorption bands around 11,000 and 14,000 cm^{-1}, a weak but broad band near 24,000 cm^{-1}, and a strong absorption band in the near-UV region at approximately 30,700 cm^{-1} (Fig. 3). In the intermediate zone of the untreated multicolored sample, the light blue (I1) portion shows only a broad OAS band at ~14,000 cm^{-1} and an intense wide band at ~11,000 cm^{-1} in the near-infrared (NIR) region (Fig. 3). The blue violetish (I2) portion, in addition to the bands at about 11,000 and 14,000 cm^{-1}, shows an absorption band at 18,800 cm^{-1} (Fig. 3). This band at approximately 19,000 cm^{-1} is also present in the terminal portion (T) of the sample, which is

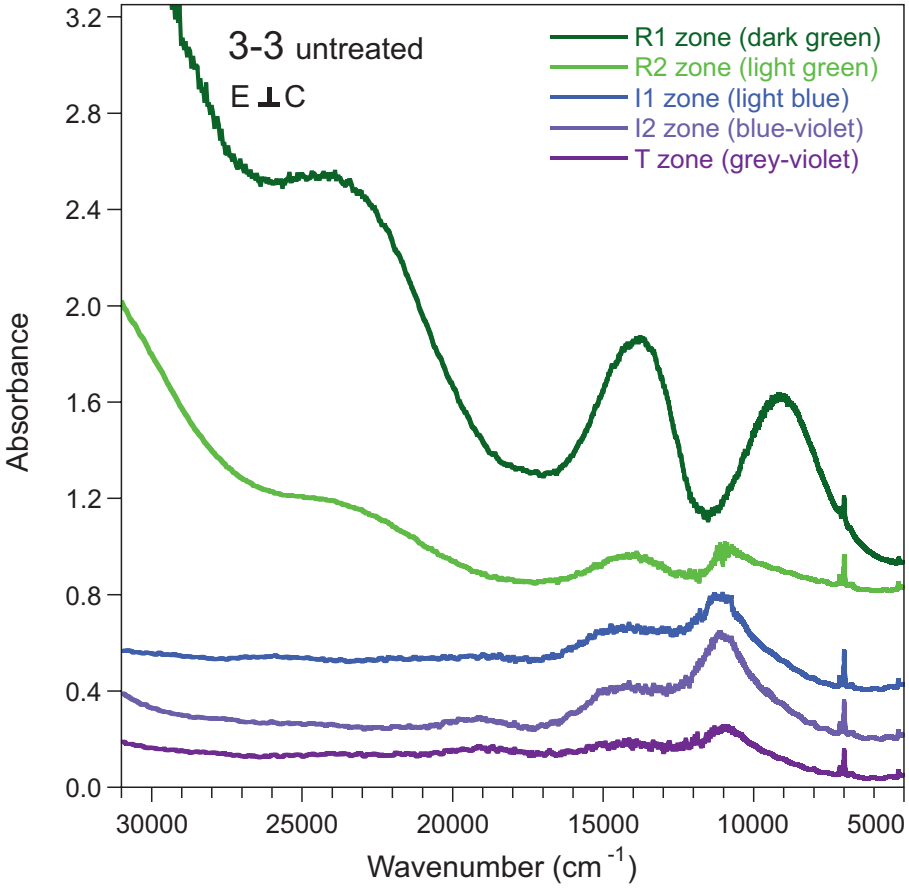


Fig. 3 OAS spectra (**E⊥c**) of the 3_3 untreated multicolored sample, from the dark green root (R1) to the greyish violet (T) terminal portion.

greyish violet in color, although the bands at 11,000 and 14,000 cm^{-1} are present and weaker there (Fig. 3). The sharp bands in the NIR region between 6,700 and 7,200 cm^{-1} are attributed to overtones of the fundamental (OH)-stretching modes (Altieri et al. 2023) (Fig. 3).

The absorption spectra recorded perpendicular to the **c**-axis in the heat-treated sample (Fig. 4) exhibit features comparable to those observed in the untreated multicolored sample. The most significant difference is the absence of the band at approximately 19,000 cm^{-1} (Fig. 4), which is present in the blue violetish (I2) and greyish violet (T) portions of the untreated multicolored sample (Fig. 3). After heat treatment, the sample displays a predominantly light blue coloration, except for the dark green root (R1) and the yellowish light green (R2) upper band, which remain essentially unchanged after heating (Fig.1).

4.3. EPR spectra

Electron paramagnetic resonance analyses were carried out on the greyish violet (T) terminal portion of the untreated sample (EPR_r sample) and on the corresponding terminal portion (T) of the heat-treated sample (EPR_t sample), which developed a light blue coloration after heating (Fig. 1).

In the EPR_r sample, the EPR spectrum acquired in a wide field range (Fig. 5) showed many broad signals in the low-field region 50–250 mT likely attributable to several Fe^{3+} centers with different low-symmetry environments (orthorhombic Fe^{3+}). Between 250 and 350 mT a complex pattern of sharp lines: zooming on this region (Fig. 6a), four, equally spaced, lines of the same intensity are observed between 260 and 320 mT. This pattern is attributable to a Cu^{2+} center, with estimated hyperfine coupling A = 11.5 mT and g-factor g = 2.34 (here denoted as "Cu_a"). The pattern does not change much upon changing the orientation of the sample (blue and brown spectra), indicating that the hyperfine and g-tensors for this center are axial, and the tensor symmetry axis is approximately perpendicular to the magnetic field, although the placement of the sample in the EPR tube was not specifically chosen to be in this way. A second Cu^{2+} four-line pattern ("Cu_b") is observed between 300 and 340, likely attributable to a Cu^{2+} center whose magnetic tensor symmetry axis is not perpendicular to the magnetic field, and whose A and g change on changing the orientation. This center could be similar or different than the previous one, and a more detailed and extended analysis should be carried out to establish this point.

The full signal in Fig. 6a results from the overlap of the two Cu^{2+} signals, and no signal attributable to Mn^{2+} is observed, which should be expected in the same field range.

Of course, no signal attributable to Mn^{3+} can be detected at X-band, which is consistent with the fact that Mn^{3+}, having an integer spin (S = 2 in octahedral coordination; Manning 1973; Reddy et al. 2007; Strassner et al. 2023) and strong magnetic anisotropy, forms an even-spin system with magnetic transitions that are either forbidden or too weak to be detected by EPR.

In the heat-treated light blue sample EPR_t, in contrast, an additional signal seems to be overlapped with the Cu^{2+} signals. However, due to spectral complexity, its attribution remains challenging and is only tentatively assigned to Mn^{2+}. The complex pattern of EPR_t

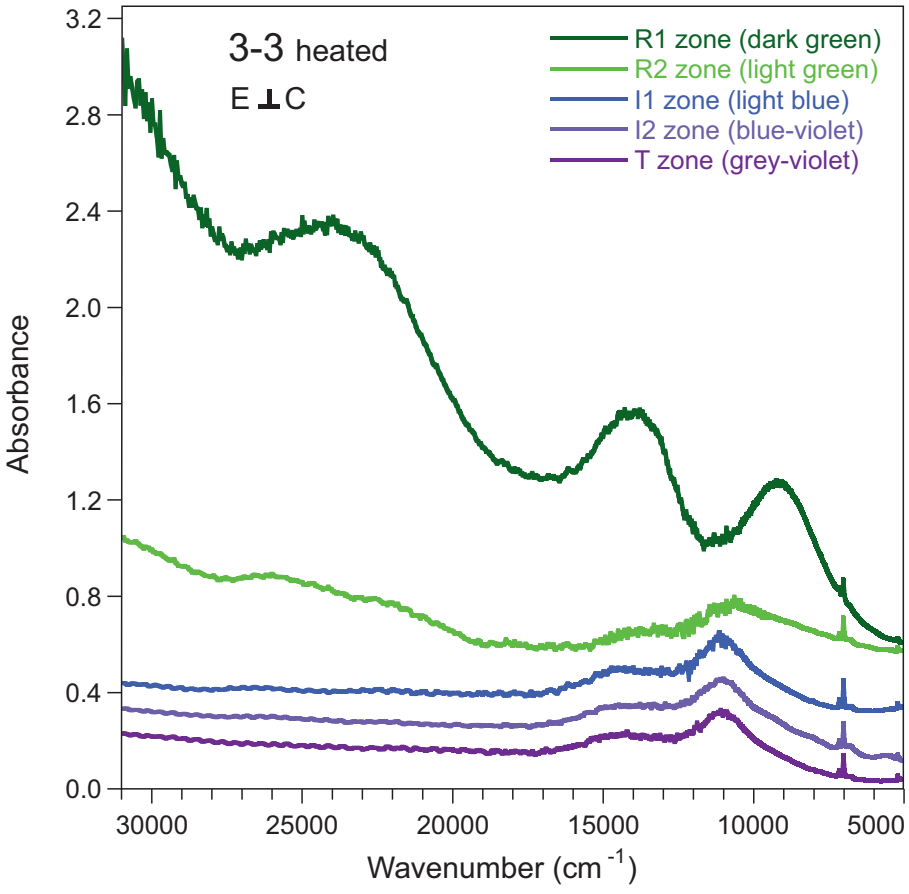


Fig. 4 OAS spectra (**E⊥c**) of the 3_3 sample heated at 500 °C for 18 hours, in the UV-Vis-NIR and visible region.

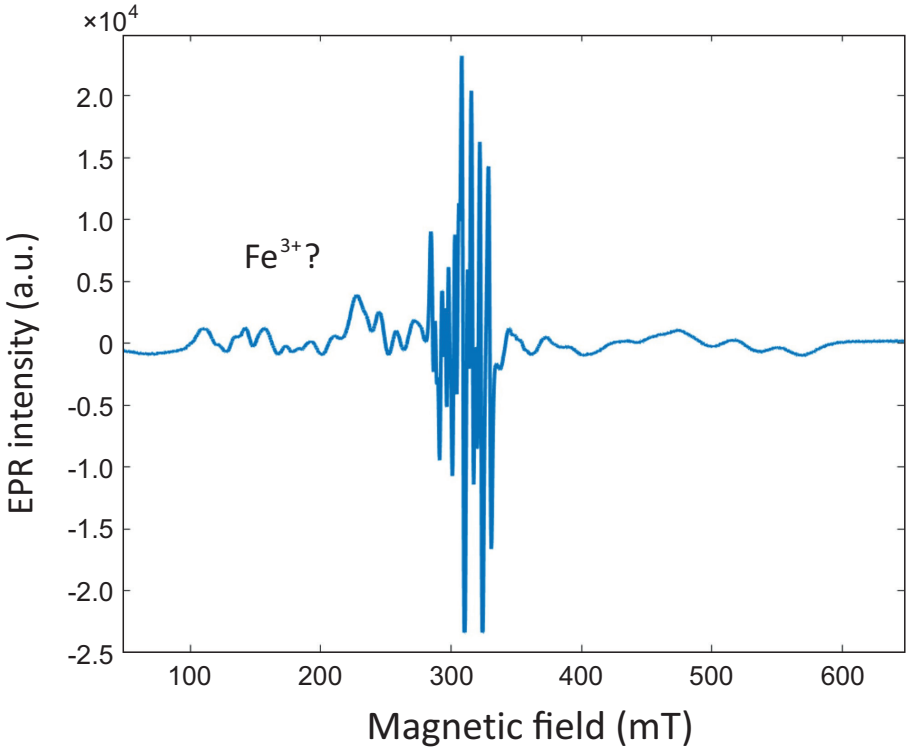


Fig. 5 EPR spectrum of the T terminal portion of the untreated reference sample, wide magnetic range.

can be disentangled powdering a small amount of EPR_t, whose EPR spectrum results in an "average" signal easier to be interpreted. Furthermore, both Q-band and X-band spectra of this powdered sample were acquired, since at Q-band Mn^{2+} signals are enhanced. The spectra are shown in Supplementary Materials with their simulations (Fig. S1 Q-band and Fig. S2 X-band, experimental spectra in blue, simulations in red). The parameters from the simulations are reported in Tab. S1. As one can see, the Q-band spectrum of the powder sample shows the typical six-line pattern expected for Mn^{2+}, confirming its presence, but the EPR parameters for this Mn^{2+} center, obtained from the simulation, indicate a pretty high D value (660 MHz), together with a slightly high g-value (2.020), suggesting a center distorted from the octahedral symmetry, with a pattern which is mainly hidden beneath the main Cu^{2+} signal in the EPR spectrum in X-band. The spectral parameters of the Mn^{2+} center indicate that this ion is localized at the *Y* site of the tourmaline structure. The octahedral coordination at this site is more distorted than at the *Z* site (Bosi 2018), with one bond significantly longer than the other five. Furthermore, as three *Y* sites are grouped to form edge-sharing [^{Y}(AlLiMn)O_{13}] units, local structural disorder associated with the occupancy of the *Y* site by cations of different size and charge (Burns et al. 1994) produces strongly asymmetric *Y*–O environments. Under these conditions, Mn^{2+} is likely displaced from the polyhedral center, occupying an off-center position.

4.4. Determination of atoms per formula unit (apfu)

The wt. % of element oxides obtained by EMPA (Tabs 1 and 2) was used to calculate the *apfu*. The B content was assumed to be stoichiometric (B = 3.00 *apfu*). Lithium was calculated following the procedure of Pesquera et al. (2016). The oxidation state of Mn and Cu was determined by OAS and EPR spectroscopy (Tab. 3). The oxidation state of Fe in the dark green root portion (R1) and yellowish light green (R2) zone was determined by OAS. Although Fe^{3+} is present in the studied samples, quantification of the Fe^{3+}/Fe_{tot} ratio is not straightforward because its signal intensities in the OAS spectra were too weak. Consequently, Fe is assumed to occur entirely as Fe^{2+} in the calculation of the chemical formulae, although Fe^{3+} is considered to be present in trace amounts. The (OH) content was calculated by charge balance, assuming (T+Y+Z) = 15.00 *apfu* and 31 anions.

The empirical formulae (Tabs 4 and 5) for the different colored zones of the 3_3 Cu-bearing tourmaline sample were calculated following the site-allocation scheme recommended by Henry et al. (2011). Results show that the chemical composition of the R1 root, R2, I1, I2 intermediate zones up to the T terminal portion of the untreated sample, is consistent with the fluor-elbaite species, ideally $Na(Li_{1.5}Al_{1.5})Al_6Si_6O_{18}(BO_3)_3(OH)_3F$.

Specifically (Fig. 2; Tabs 1 and 4), the dark green root portion (R1) corresponds to an Fe-rich, Ti-, Mn-bearing fluor-elbaite. The overlying yellowish light green band

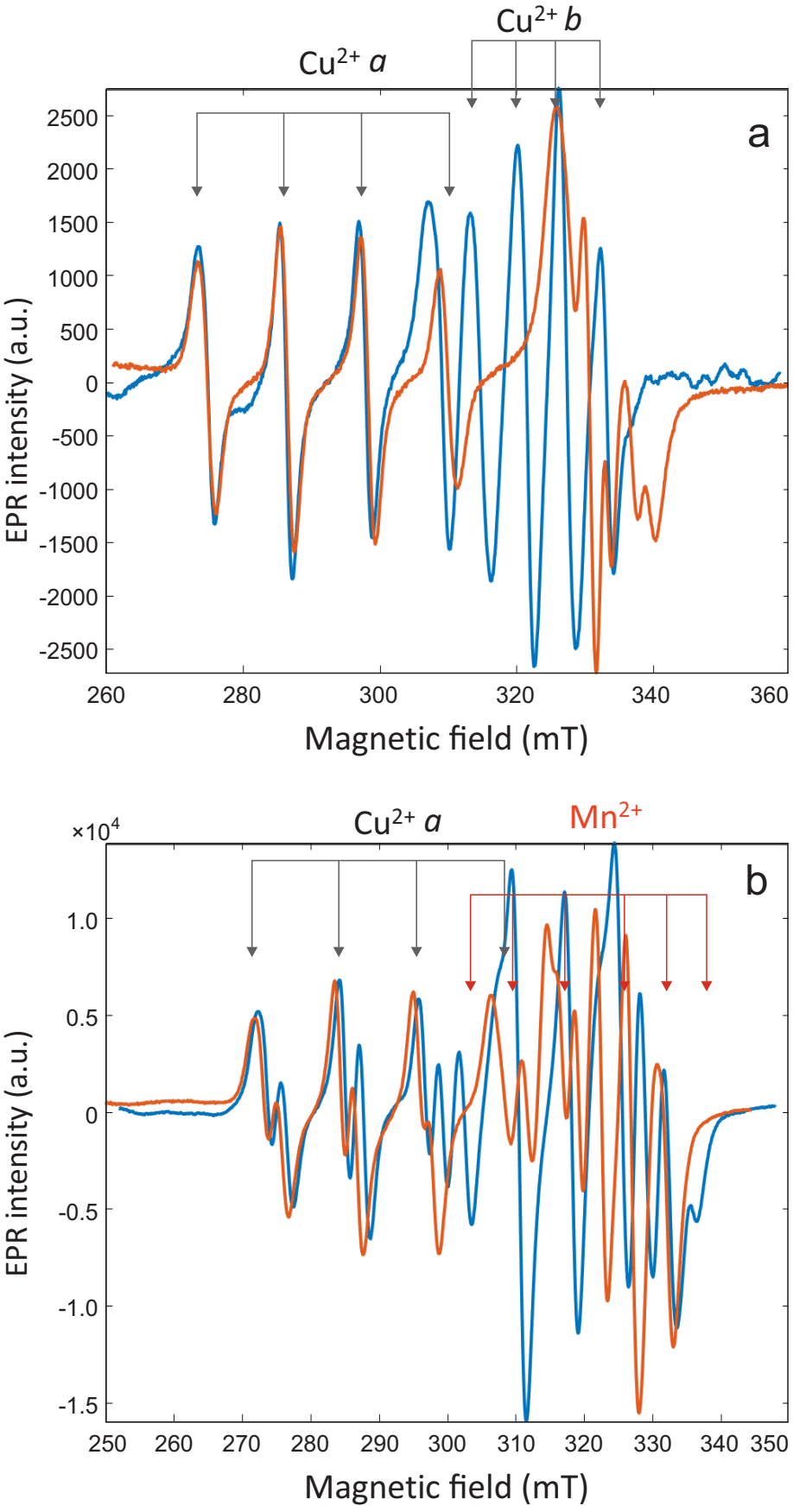


Fig. 6 EPR spectra of the T terminal portion of the sample before (a) and after (b) thermal treatment at 500 °C for 18 hours, for two orientations (blue and orange spectra) with respect to the magnetic field. The spectra are shown in the field range where Cu(II) and Mn(II) signals are expected.

Tab. 3 OAS band assignments for selected spot analyses of differently colored zones in the 3_3 untreated and heat-treated tourmaline sample.

Multicolored Cu-bearing tourmaline of Mozambique				
Before Heating	*Chemical Composition*	*Absorption Bands and Assignments*	*After Heating*	*Absorption Bands and Assignments*
Greyish Violet (T)	CuO ~0.16 wt. % MnO_{tot} ~0.24 wt. % FeO_{tot} ~0.01 wt. % TiO_2 ~0.01 wt. %	*~ 19,000 cm^{-1}* = Mn^{3+} *d–d* transitions *~ 14,000 cm^{-1}* = Cu^{2+} *d–d* transitions *~ 11,000 cm^{-1}* = Cu^{2+} *d–d* transitions	Light Blue 3 (T)	*~ 14,000 cm^{-1}* = Cu^{2+} *d–d* transitions *~ 11,000 cm^{-1}* = Cu^{2+} *d–d* transitions
Blue Violetish (I2)	CuO ~0.30 wt. % MnO_{tot} ~0.08 wt. % FeO_{tot} ~0.00 wt. % TiO_2 ~0.01 wt. %	*~ 19,000 cm^{-1}* = Mn^{3+} *d–d* transitions *~ 14,000 cm^{-1}* = Cu^{2+} *d–d* transitions *~ 11,000 cm^{-1}* = Cu^{2+} *d–d* transitions	Light Blue 2 (I2)	*~ 14,000 cm^{-1}* = Cu^{2+} *d–d* transitions *~ 11,000 cm^{-1}* = Cu^{2+} *d–d* transitions
Light Blue (I1)	CuO ~0.26 wt. % MnO_{tot} ~0.06 wt. % FeO_{tot} ~0.03 wt. % TiO_2 ~0.01 wt. %	*~ 14,000 cm^{-1}* = Cu^{2+} *d–d* transitions *~ 11,000 cm^{-1}* = Cu^{2+} *d–d* transitions	Light Blue (I1)	*~ 14,000 cm^{-1}* = Cu^{2+} *d–d* transitions *~ 11,000 cm^{-1}* = Cu^{2+} *d–d* transitions
Yellowish Light Green (R2)	CuO ~0.14 wt. % MnO_{tot} ~0.54 wt. % FeO_{tot} ~0.40 wt. % TiO_2 ~0.05 wt. %	*~ 30,700 cm^{-1}* = Mn^{2+}–Ti^{4+} IVCT *~ 24,000 cm^{-1}* = Fe^{2+}–Ti^{4+} IVCT *~ 14,000 cm^{-1}* = Cu^{2+} *d–d* transitions *~ 11,000 cm^{-1}* = Cu^{2+} *d–d* transitions	Yellowish Light Green (R2)	*~ 30,700 cm^{-1}* = Mn^{2+}–Ti^{4+} IVCT *~ 24,000 cm^{-1}* = Fe^{2+}–Ti^{4+} IVCT *~ 14,000 cm^{-1}* = Cu^{2+} *d–d* transitions *~ 11,000 cm^{-1}* = Cu^{2+} *d–d* transitions
Dark Green Root (R1)	CuO ~0.05 wt. % MnO_{tot} ~0.49 wt. % FeO_{tot} ~1.81 wt. % TiO_2 ~0.12 wt. %	*~ 24,000 cm^{-1}* = Fe^{2+}–Ti^{4+} IVCT *~ 9,200 cm^{-1}* = Fe^{3+}–Fe^{2+} exchange-coupled pairs *~ 13,800 cm^{-1}* = Fe^{3+}–Fe^{2+} exchange-coupled pairs	Dark Green Root (R1)	*~ 24,000 cm^{-1}* = Fe^{2+}–Ti^{4+} IVCT *~ 9,200 cm^{-1}* = Fe^{3+}–Fe^{2+} exchange-coupled pairs *~ 13,800 cm^{-1}* = Fe^{3+}–Fe^{2+} exchange-coupled pairs

(R2) is characterized by higher Mn contents, with minor amounts of Ti and Fe. The intermediate light blue zone (I1) represents an Cu^{2+}-, Mn^{2+}-bearing fluor-elbaite, whereas the blue violetish zone (I2), with slightly higher Cu contents, is characterized by Mn predominantly in the +3 oxidation state. In the terminal greyish violet fluor-elbaite (T) portion, Cu contents decrease, while Mn increases and it occurs in both Mn^{2+} and Mn^{3+} oxidation states.

The EMP analyses performed on sample 3_3 after heat treatment confirm the compositional trends observed in the untreated sample and allow the calculation of empirical formulae that are nearly identical for the untreated and treated samples (Tabs 2 and 5).

5. Discussion

Compositional analyses of the differently colored zones revealed no detectable concentration of V_2O_3 or Cr_2O_3 (≤ 0.03 wt. %) (Tabs 1 and 2). Therefore, the transition metals responsible for coloration in this Cu-bearing tourmaline are Cu, Fe, Mn, and Ti. The untreated multicolored sample displays a continuous range of colors, from dark green at the root through yellowish light green, light blue, and blue violetish, up to the greyish violet terminal portion. The transitions are gradual rather than sharp, with the strongest blending occurring in the intermediate blue violetish zone (Fig. 1).

The OAS spectrum of the dark green root (R1) of both the untreated and heat-treated samples displays two strong absorption bands at 13,800 cm^{-1} and 9,200 cm^{-1}, and a weaker broad band at 24,000 cm^{-1} (Figs 3 and 4). The two strong bands at 13,800 and 9,200 cm^{-1} are attributed to electronic exchange interactions between Fe^{2+}/Fe^{3+} pairs located at adjacent *Y* sites in the tourmaline structure (Taran and Rossman 2002; Altieri et al. 2024). The broad band around ~24,000 cm^{-1} can be assigned to Fe^{2+}–Ti^{4+} IVCT mechanism (Mattson and Rossman 1987; Andreozzi et al. 2025). These features are consistent with the relatively high Fe (FeO ~2.0 wt. %) and Ti contents (TiO_2 ~0.12 wt. %), which are the highest observed within the sample (Fig. 2; Tab. 1). Accordingly, the dark green coloration of the crystal root is primarily controlled by Fe^{2+}/Fe^{3+} interactions and Fe^{2+}–Ti^{4+} IVCT (Tab. 3).

Above the dark green root (R1) occurs a yellowish light green (R2) zone whose OAS spectrum exhibits a broad absorption band in the near-UV region at ~30,700 cm^{-1} and a weaker broad band near 24,000 cm^{-1} (Fig. 3). These bands are attributable to Mn^{2+}–Ti^{4+} IVCT and to Fe^{2+}–Ti^{4+} IVCT, respectively (Fig. 3; Tab. 3) (Rossman and Mattson 1986; Mattson and

Tab. 4 Empirical formulae for the different coloured zones of the 3_3 untreated tourmaline sample investigated

Coloured zones	Empirical formulae
Dark Green root (R1)	$^{X}(Na_{0.65}\square_{0.32}Ca_{0.03})_{\Sigma1.00}{}^{Y}(Al_{1.48}Li_{1.15}Fe^{2+}{}_{0.24}Mn^{2+}{}_{0.07}Cu_{0.01}Ti_{0.01})_{\Sigma3.00}{}^{Z}Al_{6.00}{}^{T}(Si_{6.05}O_{18})(BO_3)_3{}^{V}(OH)_3{}^{W}[F_{0.52}(OH)_{0.31}O_{0.17}]_{\Sigma1.00}$
Yellowish Light Green (R2)	$^{X}(Na_{0.60}\square_{0.33}Ca_{0.07})_{\Sigma1.00}{}^{Y}(Al_{1.56}Li_{1.26}Fe^{2+}{}_{0.05}Mn^{2+}{}_{0.07}Cu_{0.02}Ti_{0.01})_{\Sigma3.00}{}^{Z}Al_{6.00}{}^{T}(Si_{6.04}O_{18})(BO_3)_3{}^{V}(OH)_3{}^{W}[F_{0.77}(OH)_{0.09}O_{0.14}]_{\Sigma1.00}$
Light Blue (I1)	$^{X}(Na_{0.58}\square_{0.39}Ca_{0.03})_{\Sigma1.00}{}^{Y}(Al_{1.69}Li_{1.27}Cu_{0.03}Mn^{2+}{}_{0.01})_{\Sigma3.00}{}^{Z}Al_{6.00}{}^{T}(Si_{6.00}O_{18})(BO_3)_3{}^{V}(OH)_3{}^{W}[F_{0.61}(OH)_{0.30}O_{0.09}]_{\Sigma1.00}$
Blue Violetish (I2)	$^{X}(Na_{0.56}\square_{0.37}Ca_{0.07})_{\Sigma1.00}{}^{Y}(Al_{1.69}Li_{1.26}Cu_{0.04}Mn^{3+}{}_{0.01})_{\Sigma3.00}{}^{Z}Al_{6.00}{}^{T}(Si_{6.01}O_{18})(BO_3)_3{}^{V}(OH)_3{}^{W}[F_{0.61}(OH)_{0.22}O_{0.17}]_{\Sigma1.00}$
Greyish Violet (T)	$^{X}(Na_{0.59}\square_{0.37}Ca_{0.04})_{\Sigma1.00}{}^{Y}(Al_{1.67}Li_{1.28}Cu_{0.02}Mn^{2+}{}_{0.02}Mn^{3+}{}_{0.02})_{\Sigma3.00}{}^{Z}Al_{6.00}[{}^{T}(Si_{5.99}Al_{0.01})_{\Sigma6.00}O_{18}](BO_3)_3{}^{V}(OH)_3{}^{W}[F_{0.50}(OH)_{0.44}O_{0.06}]_{\Sigma1.00}$

Rossman 1987). Compositional data are consistent with the presence, in this zone, of Fe (~0.40 wt. % as FeO) and Ti (~0.05 wt. % as TiO_2), along with enrichment in MnO (~0.54 wt. %), representing the highest Mn concentrations measured in the entire sample (Tab. 1; Fig. 2). Additionally, very weak absorption bands at ~11,000 and ~14,000 cm^{-1} are also present in the spectrum of the yellowish light green (R2) portion, both attributable to Cu^{2+} spin-allowed *d–d* electronic transitions (Fig. 3) (Rossman et al. 1991; Mashkovtsev et al. 2006). These weak absorption bands are consistent with the low CuO contents in this zone (0.05–0.14 wt. %), which results in only a very faint bluish shade (Fig. 2; Tab. 1).

In the intermediate zone of the untreated sample (light blue I1 and blue violetish I2 zones), Cu progressively increases (CuO = 0.26–0.30 wt. %), whereas Fe decreases significantly, with FeO values below the EMP detection limit (Fig. 2; Tab. 1). TiO_2 also decreases to below detection levels (Fig. 2; Tab. 1). The MnO content (~0.06 wt. %) is below the threshold (1–3 wt. %) required to produce detectable Mn^{2+} spin-forbidden bands (Reinitz and Rossman 1988; Taran et al. 1993; Rossman 2014) and the lack of TiO_2 precludes Mn^{2+}–Ti^{4+} IVCT (Fig. 3; Tab. 1). The OAS spectrum of the light blue (I1) zone, recorded perpendicular to the **c**-axis, shows only a broad band at ~14,000 cm^{-1} and an intense band at ~11,000 cm^{-1} in the near-infrared, both corresponding to Cu^{2+} spin-allowed *d–d* electronic transitions (Fig. 3). Thus, in the I1 zone, Fe, Mn, and Ti do not contribute to coloration and Cu^{2+} is the sole chromophore (Tab. 3). This light blue zone can therefore be classified as Paraíba-type tourmaline, as can be the upper blue violetish (I2) zone (Fig. 1).

Although the most appreciated and highly prized Paraíba tourmalines typically exhibit colors ranging from turquoise green to neon blue, the present blue violetish Cu-bearing tourmalines can also be classified as Paraíba. In fact, according to the Laboratory Manual Harmonization Committee (LMHC) guidelines, the term "Paraíba" refers to Cu-bearing elbaitic crystals whose color is primarily caused by Cu^{2+}, with the presence of Mn, as shown by our sample. Blue violetish hues, however, are less valued on the gem market.

In the I2 region of the untreated sample, the transition from blue to violet is gradual and diffuse (Fig. 1). The OAS spectrum perpendicular to the **c**-axis shows, in addition to the Cu^{2+} absorption bands at ~11,000 and ~14,000 cm^{-1}, a distinct band at 18,800 cm^{-1} attributable to Mn^{3+} spin-allowed *d–d* electronic transitions (Fig. 3; Tab. 3) (Reinitz and Rossman 1988; Taran et al. 1993; Ertl et al. 2005; Luppi et al. 2026). Unlike Mn^{2+}, a weak absorber with barely detectable OAS features, Mn^{3+} is an intense absorber, typically producing red color in tourmaline (Reinitz and Rossman 1988; Taran et al. 1993; Rossman 2014; Luppi et al. 2026). In the OAS spectrum of the blue violetish (I2) zone, Mn^{3+} strongly absorbs in the green region, weakly in the blue, and in the UV, whereas Cu^{2+} absorbs in the infrared and in the red region (Fig. 3). The combination of these absorptions generates two transmission windows: one around 22,000 cm^{-1} (blue-violet) and another near 17,000 cm^{-1} (orange) (Fig. 3). Their mixing yields the observed blue violetish color (Fig. 1). Based on the intensity of the Mn^{3+} absorption band at ~19,000 cm^{-1}, recorded perpendicular to the **c**-axis (Fig. 3), the proportion of trivalent manganese was estimated. The calculation used the molar absorption coefficient proposed by Reinitz and Rossman (1988). However, this coefficient may be up to four times higher, as shown by Bosi et al. (2021). Taking this into account, the results indicate that a very large fraction of Mn is present in the trivalent oxidation state (Tab. 1). Given the low total MnO content (approximately 0.08 wt. %), it can therefore be concluded that, particularly in the more purplish regions, a substantial proportion of Mn^{2+} is oxidized to Mn^{3+} (Fig. 3; Tabs 1 and 4).

The ~19,000 cm^{-1} band attributed to Mn^{3+} is also present in the terminal greyish violet (T) zone of the untreated sample (Fig. 3). In this area, the Cu^{2+} bands at 11,000 and 14,000 cm^{-1} are observed too (Fig. 3; Tab. 3) (Rossman et al. 1991; Mashkovtsev et al. 2006), although they are weaker than in the intermediate (I1 and I2) zone, consistent with the decrease in copper content toward the crystal termination, where CuO reaches values of about 0.16 wt. % (Fig. 2; Tab. 1). Based on the intensity of the ~19,000 cm^{-1} Mn^{3+} band and the molar extinction coefficient reported by Reinitz and Rossman (1988), the Mn^{3+} content is estimated to be 0.099 wt. %, corresponding to 53 % of the total Mn (Mn_{tot} = 0.19 wt. %). Thus, approximately half of the Mn^{2+} is oxidized to Mn^{3+}. The resulting greyish violet color is produced by the combined Mn^{3+} and Cu^{2+} absorptions (Fig. 3). Their interac-

Tab. 5 Empirical formulae for the different coloured zones of the 3_3 heated tourmaline sample investigated

Coloured zones	Empirical formulae
Dark Green root (R1)	$^{X}(Na_{0.65}\square_{0.30}Ca_{0.05})_{\Sigma 1.00}{}^{Y}(Al_{1.45}Li_{1.16}Fe^{2+}{}_{0.24}Mn^{2+}{}_{0.08}Ti_{0.02}Cu_{0.01})_{\Sigma 3.00}{}^{Z}Al_{6.00}{}^{T}(Si_{6.05}O_{18})(BO_3)_3{}^{V}(OH)_3{}^{W}[F_{0.59}(OH)_{0.22}O_{0.19}]_{\Sigma 1.00}$
Yellowish Light Green (R2)	$^{X}(Na_{0.59}\square_{0.36}Ca_{0.05})_{\Sigma 1.00}{}^{Y}(Al_{1.59}Li_{1.25}Fe^{2+}{}_{0.05}Mn^{2+}{}_{0.07}Cu_{0.01})_{\Sigma 3.00}{}^{Z}Al_{6.00}{}^{T}(Si_{6.03}O_{18})(BO_3)_3{}^{V}(OH)_3{}^{W}[F_{0.61}(OH)_{0.28}O_{0.11}]_{\Sigma 1.00}$
Light Blue (I1)	$^{X}(Na_{0.58}\square_{0.40}Ca_{0.02})_{\Sigma 1.00}{}^{Y}(Al_{1.70}Li_{1.26}Cu_{0.03}Mn^{2+}{}_{0.01})_{\Sigma 3.00}{}^{Z}Al_{6.00}{}^{T}(Si_{6.01}O_{18})(BO_3)_3{}^{V}(OH)_3{}^{W}[F_{0.59}(OH)_{0.33}O_{0.08}]_{\Sigma 1.00}$
Blue Violetish (I2)	$^{X}(Na_{0.55}\square_{0.40}Ca_{0.05})_{\Sigma 1.00}{}^{Y}(Al_{1.69}Li_{1.26}Cu_{0.03}Mn^{2+}{}_{0.01})_{\Sigma 3.00}{}^{Z}Al_{6.00}{}^{T}(Si_{6.01}O_{18})(BO_3)_3{}^{V}(OH)_3{}^{W}[F_{0.51}(OH)_{0.40}O_{0.09}]_{\Sigma 1.00}$
Greyish Violet (T)	$^{X}(Na_{0.53}\square_{0.42}Ca_{0.05})_{\Sigma 1.00}{}^{Y}(Al_{1.67}Li_{1.27}Cu_{0.03}Mn^{2+}{}_{0.02})_{\Sigma 3.00}{}^{Z}Al_{6.00}{}^{T}(Si_{6.00}O_{18})(BO_3)_3{}^{V}(OH)_3{}^{W}[F_{0.60}(OH)_{0.35}O_{0.05}]_{\Sigma 1.00}$

tion generates transmission windows in the blue-violet and yellow-orange regions with comparable intensity, creating an additive mixture perceived as greyish violet (Fig. 1). The presence of Mn^{3+} in both the blue violetish (I2) and greyish violet (T) zones likely results from oxidation of Mn^{2+} by natural radiation, probably from radioactive fluids, during the final stages of tourmaline crystallization. This process is discussed in detail in the section "Potential natural mechanisms responsible for $Mn^{2+} \rightarrow Mn^{3+}$". Narrow NIR bands between 6,700–7,200 cm^{-1} correspond to overtones of O-H stretching region (3,300–3,700 cm^{-1}) (Bosi et al. 2025).

After heat treatment, the sample 3_3 displays a predominantly light blue coloration, except for the dark green root (R1) and yellowish light green (R2) band, which remained essentially unchanged (Fig. 1). The absorption spectra, recorded perpendicular to the **c**-axis, show features comparable to those of the untreated sample (Figs 3 and 4). The dark green coloration of the crystal root (R1) is mainly controlled by Fe^{2+}/Fe^{3+} interactions and Fe^{2+}–Ti^{4+} IVCT, with absorption bands at 13,800 and 9,200 cm^{-1}, as well as a weak broad band at 24,000 cm^{-1} (Fig. 4; Tab. 3). The yellowish light green (R2) zone after heating shows a Mn^{2+}–Ti^{4+} IVCT band at ~30,700 cm^{-1} and a weaker band near 24,000 cm^{-1} caused by Fe^{2+}–Ti^{4+} IVCT, with minor Cu^{2+}- related absorptions at ~11,000 and ~14,000 cm^{-1} (Fig. 4; Tab. 3). A markedly different behavior is observed in the intermediate and terminal zones of the sample. The untreated blue violetish (I2) and greyish violet (T) zones shifted to light blue after heating at ~500 °C under reducing conditions for 18 hours (Fig. 1). This chromatic change results from the reduction of Mn^{3+} to Mn^{2+}, as demonstrated by the disappearance of the Mn^{3+} band at ~19,000 cm^{-1} in the OAS spectra of the intermediate (I2) and terminal (T) zones of the heat-treated sample (Fig. 4) (Luppi et al. 2026). EPR spectra further indicate the presence of signals that, due to the spectral complexity, are tentatively attributed to Mn^{2+} in these areas of the heat-treated light blue sample (Fig. 6b). Note that as Mn^{2+} is a weak absorber and the total MnO content is below the threshold required to detect Mn^{2+} absorptions in the OAS spectra (1–3 wt. %), it no longer contributes to the coloration. Thus, light blue color obtained after heating derives exclusively from Cu^{2+}, as indicated by the persistence of the ~11,000 and ~14,000 cm^{-1} bands (Fig. 4; Tab. 3). Cu^{2+} absorptions create a broad transmission window between ~17,000 and 24,000 cm^{-1} (≈400–580 nm), usually responsible for blue Paraíba color (Laurs et al. 2008).

5.1. Potential natural mechanisms responsible for the oxidation $Mn^{2+} \rightarrow Mn^{3+}$

The 3_3 untreated multicolored sample is a detrital fragment, which was a part of a multicolored tourmaline crystal, approximately 1.6 cm in size and of high gemological quality (Fig. 1). Its geochemical evolution suggests that such crystal formed in the central part of a pegmatite vein, most likely within a miarolitic cavity. The compositional variations observed in the crystal provide important information on the characteristics and evolution of the crystallization environment and its associated fluids. The R1 and R2 zones exhibit a marked enrichment in Fe and Mn, reflecting the high availability of these elements during the early stages of tourmaline crystallization. In contrast, the intermediate (I1–I2) and terminal (T) zones show a progressive decrease in Fe, indicating that the pegmatitic melt was depleted in Fe likely due to the tourmaline crystallization.

This Fe depletion supported Cu incorporation into the intermediate and terminal zones of the crystal. A negative correlation is observed between Cu and Fe contents ($r = -0.86$, based on 17 data points where Fe > 0.01 *apfu*). Indeed, CuO increases while FeO begins to decline, reaching maximum values of ~0.30 wt. % in the intermediate I1 and I2 zones and about 0.16 wt. % in the (T) terminal zone (Fig. 2; Tab. 1). The highest concentrations correspond to the most geochemically evolved growth sectors. The occurrence of Cu in pegmatitic systems is generally interpreted as the result of contamination of pegmatitic melts or fluids, either at the source or during emplacement (Beurlen et al. 2011; Beckett-Brown et al. 2023).

The enhanced incorporation of Cu in the intermediate zone and its subsequent decrease toward the terminal part of the sample are also influenced by the behavior of Mn along the crystal. Indeed, MnO_{tot} content decreases in the intermediate light blue (I1) zone, reaching values near the detection limit, and then increases again in the distal part of the blue violetish (I2) portion and in the

terminal greyish violet (T) zone, up to about 0.24 wt. % (Fig. 2; Tab. 1). These last two zones, characterized by negligible TiO_2 and FeO contents (0.01 wt. %), contain Mn^{3+} (Tab. 3). The occurrence of more oxidizing conditions in the zones I2 and T is difficult to reconcile with the globally reducing conditions inferred for tourmaline crystallization, as no evidence suggests a significant redox change during crystal growth that could account for a transient shift toward more oxidizing conditions in these zones.

Regarding the potential natural mechanisms responsible for the oxidation of Mn^{2+} to Mn^{3+} in the blue violetish (I2) and greyish violet (T) portions of the crystal, three main hypotheses can be considered:

1. Post-crystallization oxidation (late-stage hydrothermal alteration)
   A rupture of the miarolitic cavity, caused by brittle deformation during the final stages of pegmatite crystallization, could have partially opened the geochemical system. Highly reactive late-stage cavity fluids might have infiltrated fractures in the surrounding pegmatitic rock. Under this scenario, the tourmaline crystal would have been exposed to oxidizing fluids, leading to hydrothermal alteration that preferentially affected its outermost portions, oxidizing surface Mn^{2+} to Mn^{3+} (Altieri et al. 2024).
2. Oxidative incorporation during late growth
   A second hypothesis attributes the presence of Mn^{3+} in the I2 and T zones to a small amount of Mn^{3+} initially present in the melt. Previous studies report that the partition coefficient of Mn is anomalously low for Mn^{3+}, and that Mn incorporation in tourmaline is strongly dominated by Mn^{2+} (van Hinsberg 2011). Consequently, the Mn^{3+}/Mn^{2+} ratio would increase solely after the preferential incorporation and near-complete depletion of Mn^{2+} from the system, allowing Mn^{3+} to enter the structure only during the latest growth stages.
3. Natural ionizing radiation
   A third hypothesis is that natural ionizing radiation (γ-rays or radioactive fluids) progressively oxidized Mn^{2+} to Mn^{3+} over geologic timescales. Koivula et al. (2009), for example, suggested that pink–red zones surrounding growth tubes or fractures in Cu-bearing blue or blue-green tourmalines from Mozambique were produced by radioactive solutions infiltrating such micro-cavities by capillarity and locally irradiating the surrounding material, thereby oxidizing Mn^{2+} to Mn^{3+} and generating the observed coloration.

The first hypothesis, post-crystallization oxidation linked to partial system reopening, is considered credible in principle but can be excluded in this case. Indeed, an oxidation environment related to partial reopening of the system would be linked to some dramatic change in the overall composition of the tourmaline, which is not the case for the transition observed in the blue-violet (I2) and greyish-violet (T) zones, where Mn^{2+} is transitioning to Mn^{3+} (Figs 2 and 3; Tab. 1). This suggests the absence of a major geochemical overprint and instead implies a "gentle" redox process producing only minor, continuous compositional variations. As additional information, an abrupt and sudden change in tourmaline composition has indeed been observed linked to a pocket rupture, as described in Altieri et al. (2024), for samples collected from the Marina pegmatite, which is the only significant primary pegmatitic deposit in the Mavuco area.

Such evidence is more consistent with the other two hypotheses: late Mn partitioning and, even more convincingly, localized natural irradiation. The second hypothesis, incorporation of Mn^{3+} only after complete depletion of Mn^{2+}, is difficult to reconcile with known physicochemical constraints. Indeed, without a strong oxidizing driver in the melt (e.g., high fO_2, oxidizing fluids, etc.), a typical pegmatitic melt would not stabilize or incorporate substantial Mn^{3+}. In the 3_3 untreated multicolored sample, the transition to the blue violetish (I2) and terminal greyish violet (T) zones, where Mn^{3+} predominates, is rather gradual and does not exhibit any significant change in bulk composition that would indicate input from a Mn^{3+}-enriched melt (Fig. 2; Tab. 1). This aspect, however, must be more circumstantiated with additional study, as some information about the difference of partition coefficient in tourmaline between Mn^{2+} and Mn^{3+} has been cited by Van Hinsberg (2011).

The most likely explanation, therefore, appears to be the oxidation of Mn^{2+} to Mn^{3+} induced by natural radiation, as also supported by the studies of Altieri et al. (2024) on a multicolored tourmaline from Mozambique. Exposure to radioactive solutions in Mavuco area (Mozambique) could have occurred within the gem pockets that originally hosted the tourmalines (Koivula et al. 2009). These radioactive solutions may be related to the formation of radioactive minerals documented in several pegmatites of Alto Ligonha, Mozambique (e.g., Bettencourt Dias and Wilson 2000). Such natural irradiation could therefore represent a late, localized phenomenon associated with radioactive fluids, although it cannot be excluded that tourmaline crystallization occurred contemporaneously with the presence of these radioactive fluids within the cavity. Reinitz and Rossman (1988) suggested that the pink–red color of natural tourmalines (particularly elbaitic crystals) results from Mn^{2+} oxidation to Mn^{3+}, induced by prolonged exposure to natural radiation within pegmatites over millions of years. The close match between the optical spectra of naturally pink–red tourmalines and those of nearly colorless samples exposed in the laboratory to controlled high doses of gamma radiation indicates that the same chromatic mechanism operates:

ionizing radiation progressively oxidizes manganese, generating the characteristic optical absorptions responsible for pink to reddish colors.

To assess whether crystals could have received natural doses equivalent to laboratory conditions, Reinitz and Rossman (1988) measured radiation levels within tourmaline pockets in southern California pegmatites. The measured values allowed the calculation of cumulative doses absorbed by the minerals over geological time, which were consistent with the doses required in laboratory experiments to "restore" the pink color in previously heat-decolorized elbaitic crystals. From these observations, it was concluded that natural pink–red tourmalines were initially nearly colorless and dominated by Mn^{2+}, acquiring their coloration only after pegmatite cooling, with Mn^{3+} generated by prolonged exposure to natural radiation, such as background gamma radiation from ^{40}K.

In the present study, the hypothesis attributing Mn oxidation to the presence of natural radioactive fluids was investigated in detail. Specifically, EPR spectroscopic analyses were performed on the greyish violet (T) portion of the 3_3 untreated multicolored sample containing Mn^{3+}, as well as on the corresponding portion after thermal treatment in order to monitor Mn behavior before and after heating and to detect potential signatures of natural irradiation. The EPR analyses conducted on the greyish violet (T) portion of 3_3 untreated sample revealed the presence of Cu^{2+} ions only (although in symmetry inequivalent sites such as *Y* and *Z*, able to convey different orientation patterns with the sample rotation in the laboratory reference frame). Conversely, the investigation carried out on the T portion of the thermally treated sample (EPR_t) revealed, in addition to the previously cited Cu^{2+} signals, the clear appearance of a further signal beyond the Cu ions spectra. However, due to the spectral complexity, its attribution appears difficult and can be tentatively assigned to Mn^{2+}.

To clarify this point, a small amount of the EPR_t sample was powdered, yielding an averaged and more easily interpretable EPR signal. The acquisition of both X-band and Q-band spectra, where Mn^{2+}signals are enhanced, together with spectral simulations (Electronic Supplementary Material: Figs S1 and S2; Tab. S1), revealed the characteristic six-line pattern expected for Mn^{2+}, thus confirming its presence.

This coupled evidence, together with the comparative analysis of the OAS spectra of the untreated and heat-treated samples, suggest the activation of a reduction mechanism from Mn^{3+} to Mn^{2+} during the thermal treatment. This reduction process suppressed the absorption contributions associated with Mn^{3+}, thereby leaving Cu^{2+} as the sole origin of the light blue coloration observed in the sample after heating.

6. Conclusions

This study provides new insights into the redox-dependent color mechanisms in Cu-bearing fluor-elbaite from the Mavuco deposit (NE Mozambique), clarifying both the natural and heat-induced processes that control its chromatic evolution. The integration of chemical and spectroscopic data demonstrates that the complex color zoning of this multicolored tourmaline reflects systematic variations in the concentration and oxidation state of Cu, Mn, Fe, and Ti along the crystal growth direction. Fe^{2+}/Fe^{3+} exchange-coupled pairs and Fe^{2+}–Ti^{4+} intervalence charge-transfer interactions account for the dark green root, whereas Mn^{2+}–Ti^{4+} IVCT and Cu^{2+} *d-d* transitions explain the lighter green and blue zones. The violetish terminal colors are produced by the combined absorptions of Cu^{2+} and Mn^{3+}.

The occurrence of Mn^{3+} solely in the blue-violet and greyish-violet zones is best explained by post-crystallization oxidation of Mn^{2+} through localized exposure to natural ionizing radiation or radioactive fluids within the pegmatitic cavity, revealing the sensitivity of Mn oxidation state to subtle redox variations in pegmatitic environments. Thermal treatment under reducing conditions (~500 °C) reverses this process, reducing Mn^{3+} to Mn^{2+} and producing a homogeneous light-blue coloration. The disappearance of Mn^{3+} leaves Cu^{2+} as the sole chromophore responsible for the Paraíba-like color.

Overall, the results highlight the capacity of tourmaline to record and preserve small-scale redox gradients and subsequent post-crystallization processes. From a gemological standpoint, they provide diagnostic criteria to distinguish natural violetish coloration produced by irradiation from that resulting from artificial heat treatment, thus refining the identification of natural *versus* treated Paraíba-type tourmalines. These findings underscore the dual geological and gemological relevance of Cu-bearing tourmalines, which act both as petrogenetic indicators of redox evolution in pegmatitic systems and as natural archives of radiation-induced processes governing their color diversity.

Acknowledgements. Funding by Sapienza University of Rome (Prog. "Avvio alla Ricerca" 2025 to R. L., and Prog. Università 2025 to F. B.) is gratefully acknowledged. FDB acknowledges the Università di Ferrara for funding this research under the FAR2025 programme. We thank the editors for the efficient and careful handling of the manuscript, as well as the reviewers (Andreas Ertl and an anonymous reviewer) for their constructive and helpful comments.

References

Agrosì G, Bosi F, Lucchesi S, Melchiorre G, Scandale E (2006) Mn-tourmaline crystals from island of Elba (Italy): Growth history and growth marks. Am mineral 91: 944–952

Altieri A, Luppi R, Skogby H, Hålenius U, Tempesta G, Pezzotta F, Bosi F (2023) Thermal treatment of the tourmaline Fe-rich princivalleite $Na(Mn_2Al)Al_6(Si_6O_{18})(BO_3)_3(OH)_3O$. Phys Chem Miner 50: 27

Altieri A, Pezzotta F, Skogby H, Hålenius U, Bosi F (2024). Tourmaline as a petrogenetic indicator highlighted in a multicoloured crystal from the gem deposit of Mavuco, Alto Ligoña pegmatite district, NE Mozambique. Mineral Mag 88(6): 745–754

Andreozzi GB, Gori C, Skogby H, Hålenius U, Altieri A, Bosi F (2025). Insights from the compositional evolution of a multi-coloured, zoned tourmaline from the Cruzeiro pegmatite, Minas Gerais, Brazil. Eur J Mineral 37(1): 1–12

Beckett-Brown C, McDonald AM, McClenaghan MB (2023) Trace element characteristics of tourmaline in porphyry Cu systems: development and application to discrimination. Can J Mineral Petrol 61: 31–60

Bettencourt Dias M, Wilson WE (2000) Famous mineral localities: The Alto Ligonha pegmatites, Mozambique. Mineral Rec 31: 459–497

Beurlen H, De Moura OJM, Soares DR, Da Silva MRR, Rhede D (2011) Geochemical and geological controls on the genesis of gem-quality ''Paraíba Tourmaline'' in granitic pegmatites from northeastern Brazil. Canad Mineral 49: 277–300

Bosi F (2018) Tourmaline crystal chemistry. Am Mineral 103: 298–306

Bosi F, Celata B, Skogby H, Hålenius U, Tempesta G, Ciriotti ME, Bittarello E, Marengo A (2021) Mn-bearing purplish-red tourmaline from the Anjanabonoina pegmatite, Madagascar. Mineral Mag 85: 242–253

Bosi F, Pezzotta F, Skogby H, Luppi R, Ballirano P, Halenius U, Tempesta G, Agrosì G, Sejkora J (2025) Elbaite, the neotype material from Rosina pegmatite, San Piero in Campo, Elba Island, Italy. Eur J Mineral 37(4): 505–516

Burns PC, MacDonald DJ, Hawthorne FC (1994) The crystal-chemistry of manganese-bearing elbaite. Canad Mineral 32: 31–41

Dutrow BL, Henry DJ (2018) Tourmaline compositions and textures: reflections of the fluid phase. J Geosci 63: 99–110

Ertl A, Hughes JM, Pertlik F, Foit FF Jr, Wright SE, Brandstätter F, Marler B (2002) Polyhedron distortions in tourmaline. Canad Mineral 40: 153–162

Ertl A, Rossman GR, Hughes JM, Prowatke S, Ludwig T (2005) Mn-bearing "oxy-rossmanite" with tetrahedrally coordinated Al and B from Austria: Structure, chemistry and infrared and optical spectroscopic study. Am mineral 90: 481–487

Fritsch E, Rossman GR (1987) An update on color in gems. Part 1: Introduction and colors caused by dispersed metal ions. Gems Gemol 23(3): 126–139

Henry DJ, Dutrow BL (2011) The incorporation of fluorine in tourmaline: Internal crystallographic controls or external environmental influences? Canad Mineral 49: 41–56

Henry DJ, Novák M, Hawthorne FC, Ertl A, Dutrow B, Uher P, Pezzotta F (2011) Nomenclature of the tourmaline supergroup minerals. Am mineral 96: 895–913

Koivula JI, Nagle K, Shen AHT, Owens P (2009) Solution-Generated Pink Color Surrounding Growth Tubes and Cracks in Blue to Blue-Green Copper-Bearing Tourmalines from Mozambique. Gems Gemol 45(1): 44–47

Lächelt S (2004) The Geology and Mineral Resources of Mozambique. National Directorate of Geology, Maputo, Mozambique, pp 1–515

Laurs BM, Zwaan JC, Breeding CM, Simmons WB, Beaton D, Rijsdijk KF, Befi R, Falster AU (2008) Copper-bearing (Paraíba-type) tourmaline from Mozambique. Gems Gemol 44: 4–30

Li M, Hong H, Yin K, Wang C, Cheng F, Fang Q (2018) The Chemical States of Color-Induced Cations in Tourmaline Characterized by X-Ray Photoelectron Spectroscopy. J Spectrosc ID 3964071 DOI 10.1155/2018/3964071

Luppi R, Skogby H, Hålenius U, Di Benedetto F, Tempesta G, Vadrucci M, Agrosì G, Sejkora J, Pezzotta F, Bosi F (2026) Redox-induced color changes in Mn-bearing elbaite after electron irradiation and thermal treatments. Am mineral DOI 10.2138/am-2025-10085

Manning PG (1973) Effect of second nearest neighbouring interaction on Mn^{3+} in pink and black tourmalines. Canad Mineral 11: 971–977

Mashkovtsev RI, Smirnov SZ, Shigley JE (2006) The features of the Cu2+-entry into the structure of tourmaline. J Struct Chem 47(2): 252–257

Mattson SM, Rossman GR (1987) Fe^{2+}–Fe^{3+} interactions in tourmaline. Phys Chem Miner 14: 163–171

Pesquera A, Gil-Crespo PP, Torres-Ruiz F, Torres-Ruiz J, Roda-Robles E (2016) A multiple regression method for estimating Li in tourmaline from electron microprobe analyses. Mineral Mag 80: 1129–1133

Pezzotta F (2018) Mozambique Paraíba Tourmaline Deposits: An Update. InColor, Summer 2018, pp 52–56

Pezzotta F, Laurs BM (2011) Tourmaline: The Kaleidoscopic Gemstone. Elements 7(5): 333–338

Pouchou JL, Pichoir F (1991) Quantitative analysis of homogeneous or stratified microvolumes applying the model "PAP". In: Heinrich KFJ, Newbury DE (eds) Electron Probe Quantitation. Plenum, New York, pp 31–75

Reddy BJ, Frost RL, Martens WN, Wain DL, Kloprogge JT (2007) Spectroscopic characterization of Mn-rich tourmalines. Vib Spectrosc 44: 42–49

Reinitz I, Rossman GR (1988) Role of natural radiation in tourmaline coloration. Am mineral 73: 822–825

Rossman GR (2014) Optical Spectroscopy. Rev Mineral Geochem 78: 371–398

Rossman GR, Mattson SM (1986) Yellow, Mn-rich elbaite with Mn-Ti intervalence charge transfer. Am mineral 71: 599–602

Rossman GR, Fritsch E, Shigley JE (1991) Origin of color in cuprian elbaite from São José de Batalha, Paraíba, Brazil. Am mineral 76: 1479–1484

Strassner NM, Stipurin S, Koželj P, Grin Y, Strassner T (2023) Electronic Structure and Magnetic Properties of a High-Spin MnIII Complex: [Mn(mesacac)3] (mesacac=1,3-Bis(2,4,6- trimethylphenyl)-propane-1,3-dionato). Chem Phys Chem e202200652 DOI 10.1002/cphc.202200652

Taran MN, Rossman GR (2002) High-temperature, high-pressure optical spectroscopic study of ferric iron-bearing tourmaline. Am mineral 87: 1148–1153

Taran MN, Lebedev AS, Platonov AN (1993) Optical absorption spectroscopy of synthetic tourmalines. Phys Chem Mineral 20: 209–220

van Hinsberg VJ (2011) Preliminary experimental data on trace-element partitioning between tourmaline and silicate melt. Canad Mineral 49: 153–163